Materials Today Communications 56 (2026) 116240

Contents lists available at ScienceDirect

Materials Today Communications

journal homepage: www.elsevier.com/locate/mtcomm

Self-healing adhesives for load bearing composite structures: Computational analysis and performance prediction

Antonios Tempelis [a,*], Nicolò Truschelli [b], Laura Simonini [b,c], Alessandro Pegoretti [b,c], Andrea Dorigato [b,c], Leon Mishnaevsky Jr. [a]

[a] Department of Wind and Energy Systems, Technical University of Denmark, Roskilde, 4000, Denmark
[b] Department of Industrial Engineering, University of Trento, via Sommarive 9, Trento, 38123, Italy
[c] National Interuniversity Consortium of Materials Science and Technology (INSTM), Via Giusti 9, Florence, 50121, Italy

ARTICLE INFO

Keywords:
Adhesives
Self-healing
Finite element modelling
Single lap shear
Thermoplastics

ABSTRACT

This paper deals with modelling damage and self-healing mechanisms at the microstructural level of thermosetting/thermoplastic adhesives, and predicting the adhesive material's performance in single lap shear joints. Focus is placed on the effects of glass transition on the residual stresses formed in the microstructure of healed blends after heating of the materials at high temperatures, and the effect of partial filling of the crack faces with the thermoplastic healing agent. Microstructural models are used to simulate damage during loading of the virgin blends and the healing process to predict residual thermal stresses. The models provided accurate predictions for the strength and failure strain of the virgin blends and suggest that partial or imperfect healing of the crack faces by the healing agent is the main cause of reduction in tensile strength of the healed blends. A combination of a representative volume element and a full model of a single edge notch bending specimen is used to predict Mode I critical energy release rate (G_{IC}). The effect of sub-optimal healing of the crack faces on G_{IC} values is examined. The results suggest that sub-optimal filling of the crack faces can lead to significant reduction of G_{IC}. In addition, a mixed mode cohesive zone model that accounts for plastic deformation in the virgin and healed adhesives is developed and is found to be able to capture the load-displacement curves of single lap shear joins. The effect of the inclusion of thermoplastic phases and healing of the adhesives on the parameters of the cohesive zone model is examined through comparison with experimental data.

1. Introduction

Materials with self-healing properties are a promising technology which could potentially limit the need for maintenance and repair for a large variety of applications. For many structural applications, it is of particular interest to use self-healing adhesives, as adhesively bonded joints are some of the most critical and failure prone components.

One of the available technologies for formulating and manufacturing self-healing materials is through the use of thermoset/thermoplastic polymer blends (Fig. 1), as demonstrated by Luo et al. [1] and Cohades et al. [2,3]. In such blends, external heating and pressure are applied, which make the thermoplastic phase flow into damage such as cracks and voids that are formed during the loading phase. Upon solidification of the thermoplastic phase, the structural properties of the blend are restored to a sufficient degree to carry further load. Due to the thermoplastic nature of the healing agent, this process can be repeated multiple times, allowing for healing intervals after multiple damage events during the component' s service life. Recently, Truschelli et al. [4] manufactured adhesives consisting of epoxy resin (EP) /thermoplastic cyclic olefin copolymer (COC) blends and tested them to evaluate the healing efficiency at different healing temperatures. To test the suitability of those blends for structural applications, they evaluated their performance before and after healing using single lap shear (SLS) joints. One potential application of EP/COC self-healing materials is in adhesive bond lines of wind turbine blades, where debonding is a commonly observed damage mechanism, existing both as an initial post-manufacturing defect and also occurring during in-service loading. The self-healing properties in this case could allow the blade to carry further load after damage and increase the timespan between expensive major repairs. Epoxy/cyclic olefin copolymer blends have been studied as potential structural materials also by Mahmood et al. [5] and Dorigato et al. [6], while Simonini et al. [7] managed to generate

* Corresponding author.
E-mail address: atem@dtu.dk (A. Tempelis).

https://doi.org/10.1016/j.mtcomm.2026.116240
Received 4 June 2026; Received in revised form 22 September 2026; Accepted 24 September 2026
Available online 25 September 2026
2352-4928/© 2026 The Authors. Published by Elsevier Ltd. This is an open access article under the CC BY license (http://creativecommons.org/licenses/by/4.0/).

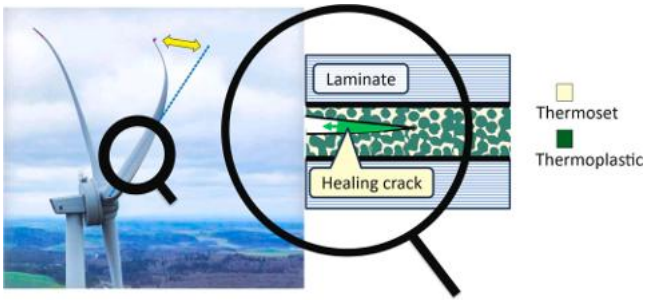


Fig. 1. Self-healing of wind turbine blade adhesive bondlines based on thermosetting/thermoplastic material blends. Heating the blend triggers flow of the thermoplastic phase and filling of microcracks and voids, restoring load carrying capacity.

self-healing interfaces by coating carbon fibers with polycaprolactone (PCL) particles. Graphene plate – reinforced microcapsules and microcapsules with nanocomposite cells have also been used to synthesize self-healing GFRP composites [8,9].

To complement experimental data and make predictions for the performance of self-healing materials for a variety of load cases, modelling and simulations tools such as the finite element (FE) method are very useful. A number of models for self-healing materials have been developed, linking the macroscopic properties of the material to a set of healing and damage variables in what is known as Continuum Damage-Healing Mechanics (CDHM). The works by Miao at al. [10], Barbero et al. [11], Al-Rub et al. [12], Darabi et al. [13], Shahsavari et al. [14], Pan et al. [15], Voyiadjis et al. [16], Esgandani et al. [17], Zhang et al. [18], Shojaei et al. [19], Ahmed et al. [20], Subramanian et al. [21] and Dai et al. [22] are examples of this kind of approach. However, these models were developed for broad application while self-healing in polymer bends offers opportunity for modelling of their microstructure, to understand how the interaction between the material phases influences the structural performance of the adhesive. For this kind of material, modelling at the microstructure level and considering the flow of the thermoplastic phase can provide accurate predictions of the post-healing performance, as demonstrated by Sun and Mishnaevsky Jr. [23] and Jahadi et al. [24]. It also offers the opportunity to examine which damage mechanisms can potentially reduce the post-healing performance.

Since adhesives are the focus of this study, Cohesive Zone Modelling (CZM) approaches [25–32] are particularly useful for modeling the behavior of adhesively bonded joints at the coupon level. CZM and self-healing have been combined in the works by Maiti et al. [33], Alsheghri and Al-Rub [34,35], Ponnusami et al. [36], Jefferson and Freeman [37] and Sun et al. [38]. Therefore, combining simulations focusing on the microstructure level, together with coupon or component level simulations which use the CZM technique to model adhesive layers, could provide great predictive capabilities for the performance of self-healing adhesives. More recent studies have focused on soft self-healing thermoplastic interlayers [39], and self-healing mechanisms in concrete [40–45] and ceramics [46].

However, in the study by Truschelli et al. [4], the healed adhesive blends, although they restored the load carrying capacity considerably, did not manage to fully restore the fracture toughness and single lap joint strength. The available literature shows that there is a general lack of computational investigations of the mechanisms that could reduce post-healing performance. Therefore, the primary purpose of the present study is to model the effects which could potentially reduce the post-healing performance using computational modelling. The two mechanisms of performance reduction that are considered are the presence of residual thermal stresses and strains that are formed during the heating process, and partial or imperfect filling of the crack faces by the healing agent. Understanding of the effects of these processes can lead to further increases in the performance of the healed adhesives and increase their competitiveness. Representative volume elements (RVE's) are used to model damage and healing at the microstructure level of the adhesives. The models are also used to model the effect of residual thermal stresses during the healing process, accounting for effects related to the glass transition temperature, and imperfect filling of the crack faces by the thermoplastic phase on the post-healing performance and relate to experimental observations. The RVE approaches can combine parameters such as the microstructure of the blends, material properties that can be obtained by relatively cheap and established experimental setups, and various material combinations to optimize the virgin (before damage) and healed adhesive properties in terms of structural performance. The RVE models can also be used to estimate mechanical properties for the adhesive blends that can provide indications for the adhesive joint performance. Such properties are the tensile strength, stiffness and Mode I critical energy release rate (G_{IC}) of the self-healing adhesives. The other focus point of this study is to develop a modelling technique based on a cohesive zone model, to capture the significant elastic-plastic deformations of the considered virgin and healed adhesives in the SLS joints, and to relate the parameters of the developed cohesive model to the effects of healing. The validity of the models developed in this study is tested through comparison with the experimental results from Truschelli et al. [4].

The study is organized as follows. In Section 2, the experimental campaign of Truschelli et al. and the measured properties are briefly summarized. In Section 3, the material models and the geometry of the EP/COC blend RVE's are described in detail. The Finite Element (FE) models used to obtain the Mode I critical energy release rate through the Single-edge-notch bending (SENB) specimen, the models considering thermal residual stresses incorporating the effects of glass transition and imperfect healing, and the SLS joint models are also described in this section. The results of the FE models and comparison with the experimental measurements are presented in Section 4.

2. Experimental campaign

This section briefly describes the experimental setups which were used to obtain tensile stress-strain curves, Mode I fracture energies, healing efficiencies, and thermal properties of the virgin and healed epoxy/COC adhesive blends. These results are explained in more detail in Truschelli et al. [4]. The materials that were tested were neat epoxy adhesive (EP), neat Cyclic Olefin Copolymer (COC), and EP/COC blends with 15% and 30% weight ratio of COC. The blends are named EP15 and EP30 for brevity. After testing, the damaged blends were healed at temperatures of 145 °C and 175 °C for 1 h and tested again to examine the post-healing performance. EP consisted of a base (Elan-tech AS 90) and a hardener (Elan-tech AW 90), mixed at weight ratio 100:45. The curing cycle consisted of 2.5 h at room temperature and 5 h at 70 °C, as recommended by the producer. As reported in the datasheet, the cured system had density of 1.08–1.12 g/cm^3 and glass transition temperature of 65–75 °C. COC (Topas 8007S-04) was used as the healing agent. It was provided by Topas Advanced Polymers GmbH (Raunheim, Germany) in form of granules of 3 mm consisting of 65 wt% of norbornene and 35 wt % of ethylene. As reported in the datasheet, it had density of 1.01 g/cm^3, Melt Flow Index (MFI) of 1.7 g/10 min (190°C, 2.16 kg) and glass transition temperature of 78 °C.

Quasi-static tensile tests (Instron 5969 - ISO 527-2 standard, crosshead speed 0.25 mm/min for measuring the elastic modulus and 1 mm/min to evaluate the strength and elongation at break) and SENB three-point bending tests (Instron 5969 – ASTM D5045 standard, 23°C, 10 kN load cell, crosshead speed 10 mm/min) were used to obtain tensile stress-strain curves, Mode I critical strain energy release rates (G_{IC}) and healing efficiencies, respectively. For the tensile tests, 1BA specimens (ISO 527) were used. For the SENB tests, specimens with dimensions 44 × 10 × 5 mm^3 were used. At least 5 samples per test method and material type were used. The healing cycle was conducted

under 145 °C or 175 °C, and 500 kPa for 1 h. The results of the quasistatic tensile tests are presented in Fig. 2a,b and the results of the three-point bending tests are summarized in Fig. 2d,e. In Fig. 2c, the tensile stress-strain curve of the CFRP material (EP0/CF) used as the adherends of the single lap shear joint is also presented.

The healing efficiency was calculated with Eq. (1), where Q is the property for which the healing efficiency is measured: Q for the virgin material and Q_H after healing. For the healing efficiency in terms of G_{IC}, the value of G_{IC} is used for Q. For the single lap shear joints, the shear strength τ_{max} of the joint is used as Q.

$$HE_Q = \frac{Q_h}{Q} \times 100\% \quad (1)$$

The thermal properties of COC (thermal conductivity, specific heat

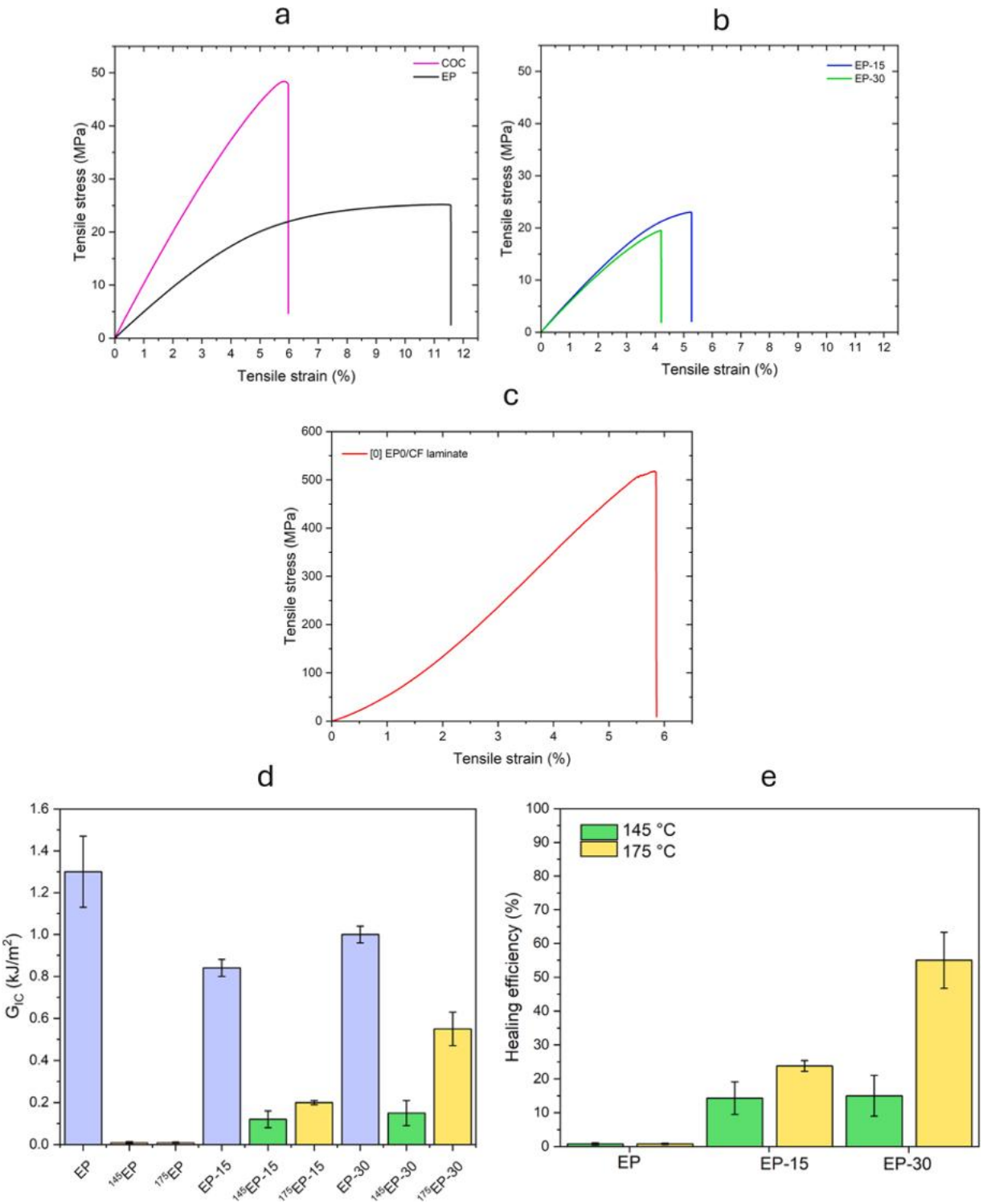


Fig. 2. Tensile stress-strain curves of the neat epoxy adhesive and COC materials (a), the virgin EP30 and EP15 blends (b), and the CFRP material used in the single lap shear joints (c). Results of the Mode I strain energy release rate from the SENB specimens, for the neat epoxy adhesive (EP), the EP15 and EP30 blends, and the healed EP and EP15 and EP30 blends at 145 °C and 175 °C (d), self-healing efficiency values (e).

capacity and coefficient of linear thermal expansion - CLTE) were obtained using Dynamic mechanical thermal analysis (DMTA) and Laser flash analysis (LFA) and are summarized in Table 1 and Table 2.

To evaluate the performance of the healed adhesive blends under loads that resemble in-service conditions, quasi-static single lap shear tests were performed. The geometry and results are summarized in Fig. 3. Woven fabric carbon fiber with an epoxy resin matrix CFRP adherends were used in the joints, whose tensile stress-strain behavior (Instron 5969 – ASTM D5868, crosshead speed 13 mm/min) is presented in Fig. 2. All laminas were unidirectional with a 0° orientation relative to the load direction. The epoxy resin system in the CFRP material (EP0) was different than the epoxy resin used in the adhesive (EP). At least five samples per adhesive case were tested. In the cases of neat EP and EP15, failure was observed to be adhesive, while failure of the adhesive was cohesive for the case of EP30. The SLS joint dimensions were $101.6 \times 25.4 \times 3.6$ mm^3 with a 25.4×12.5 mm^2 overlap.

3. Finite element modeling

3.1. Damage models for epoxy and COC

This section describes the modelling approach for simulating failure of EP and COC, using continuum damage mechanics and element failure. The input required for this approach is experimental stress-strain curves up to the point of failure under tension for the epoxy adhesive and COC. Damage models are then defined and fitted to the experimental stress-strain curves under tension, assuming that failure in the microstructure of the EP/COC material blends is driven by local tension, and thus these curves can adequately describe local failure. This assumption holds primarily when the microstructure is loaded under tension.

An elastoplastic material model (von Mises isotropic plasticity) is fitted to the tensile test data of the epoxy adhesive (Fig. 4a) and it is coupled with a ductile damage initiation and evolution law within the finite element modeling framework. In this model, damage initiates when the equivalent plastic strain reaches a critical value ε_0^{pl}, after which the stiffness of the material is degraded until no more stress can be carried, and element failure occurs. Stiffness is degraded according to a damage variable D, defined with Eq. (2):

$$D = \frac{L_c \varepsilon^{pl}}{u_f^{pl}}, u_f^{pl} = \frac{2G_f}{\sigma_{y0}} \tag{2}$$

where L_c is the characteristic element length, ε^{pl} is the equivalent plastic strain, G_f is the fracture energy of the material, and σ_{y0} is the yield stress at the point when damage initiation occurs. In this context, the fracture energy is defined with Eq. (3):

$$G_f = \int_{\varepsilon_0^{pl}}^{\varepsilon_f^{pl}} L_c \sigma_y d\varepsilon^{pl} \tag{3}$$

where ε_f^{pl} is the equivalent plastic strain when the stiffness is fully degraded, and σ_y is the yield stress as a function of equivalent plastic strain.

An in-house built code is used for fitting the elastic-plastic response and the values $E = 478.4$ MPa and $\nu = 0.43$ are used for the elastic constants, and $\sigma_y = 9.49$ MPa at the onset of plasticity. For the damage initiation and evolution parameters, we use $\varepsilon_0^{pl} = 0.055$ and $G_f = 200$ J/m^2. Single element tension under displacement-control simulations are performed and compared against the experimental curves in Fig. 4a. The FE software ABAQUS is used for the simulations.

Table 1
Coefficient of linear thermal expansion for COC.

Temperature [°C]	CLTE [K^{-1}]
-30	$0.35 \cdot 10^{-4}$
30	$0.85 \cdot 10^{-4}$
55	$0.90 \cdot 10^{-4}$

Table 2
Specific heat and thermal conductivity for COC.

Temperature range [°C]	Property	Value
25–55	Specific heat [J/g K]	1.20–1.50
25–55	Thermal conductivity [W/m K]	0.12–0.151

For COC, a linear elastic material with $E = 886.1$ MPa and $\nu = 0.4$ is used together with a maximum strain criterion to determine failure. The strain value used to determine failure is the maximum principal strain and failure occurs when it reaches a value of $\varepsilon_0 = S_{max}/E$, where $S_{max} = 49.2$ MPa is the tensile strength of COC.

Again, single element simulations are performed and the results are plotted against the experimental curve in Fig. 4b. The COC failure criterion is implemented with a user subroutines USDFLD, for cases where an implicit solver is used in ABAQUS/Standard, and with VUSDFL, for cases where an explicit solver is used in ABAQUS/Explicit. In the following micromechanical models, the interface between EP and COC is considered to have the same damage properties as EP.

3.2. Modelling the tensile behavior of EP/COC blends using representative volume elements

Representative volume elements (RVE's) of the EP/COC blends are now generated. The length of the square RVE's is chosen to be 1 mm, and the shape of the COC particles is approximated as spheres with an average radius of 127 μm, which was the average size of the COC particles used to produce the blends. The Abaqus plug-in SPATIUM [47] is used to construct 3D RVE's and apply periodic boundary conditions for all boundary faces. A uniaxial tension case is considered in all loading simulations. The minimum allowed distance between two COC particles was set to 0.01 mm and the standard deviation for the radius of the particles was set to 0.005 mm, for the construction of the RVE's.

To calculate the number of COC particles within the RVE, the volume ratio of COC, R_v, is calculated from the weight ratio R_w using Eq. (4):

$$R_V = \frac{R_w \rho_{EP}}{R_w \rho_{EP} + (1 - R_w)\rho_{COC}} \tag{4}$$

where $\rho_{EP} = 1099$ kg/m^3 and $\rho_{COC} = 983$ kg/m^3 are the densities of EP and COC, respectively. Example RVE's are shown in Fig. 4, for EP30 and EP15. The element type used for the COC particles was a 4-node linear tetrahedron (C3D4) and a 4-node linear tetrahedron, hybrid, linear pressure element type (C3D4H) was used for EP. A global element size of 0.04 mm was found to produce converged results for the stress-strain curves, and was used for all simulations. A cohesive interaction was used between the COC particles and EP matrix, with both normal and tangential stiffness values equal to 10^6 MPa/mm. For all uniaxial loading simulations, a non-linear general, static implicit solver was used, and failure was determined at the point where the computed nominal stress began to fall rapidly with small increases in applied strain.

An RVE size effect study is also conducted to observe how the RVE size affects the predictions for the macroscopic blend response. Three square RVE sizes of 0.5 mm, 0.75 mm and 1 mm are considered for the case of EP30, and three different RVE realizations are considered for each RVE size. Examples of the RVE models used for each size are presented in Fig. 5.

As the fracture properties of the EP/COC interface were not available and no interfacial failure was assumed in the previous RVE models, a parametric study is also considered where the EP/COC interface is modelled with a cohesive surface following a bilinear cohesive law. This is to investigate how failure at the interface can influence the results. The main parameters that will be varied are the peak tractions in the

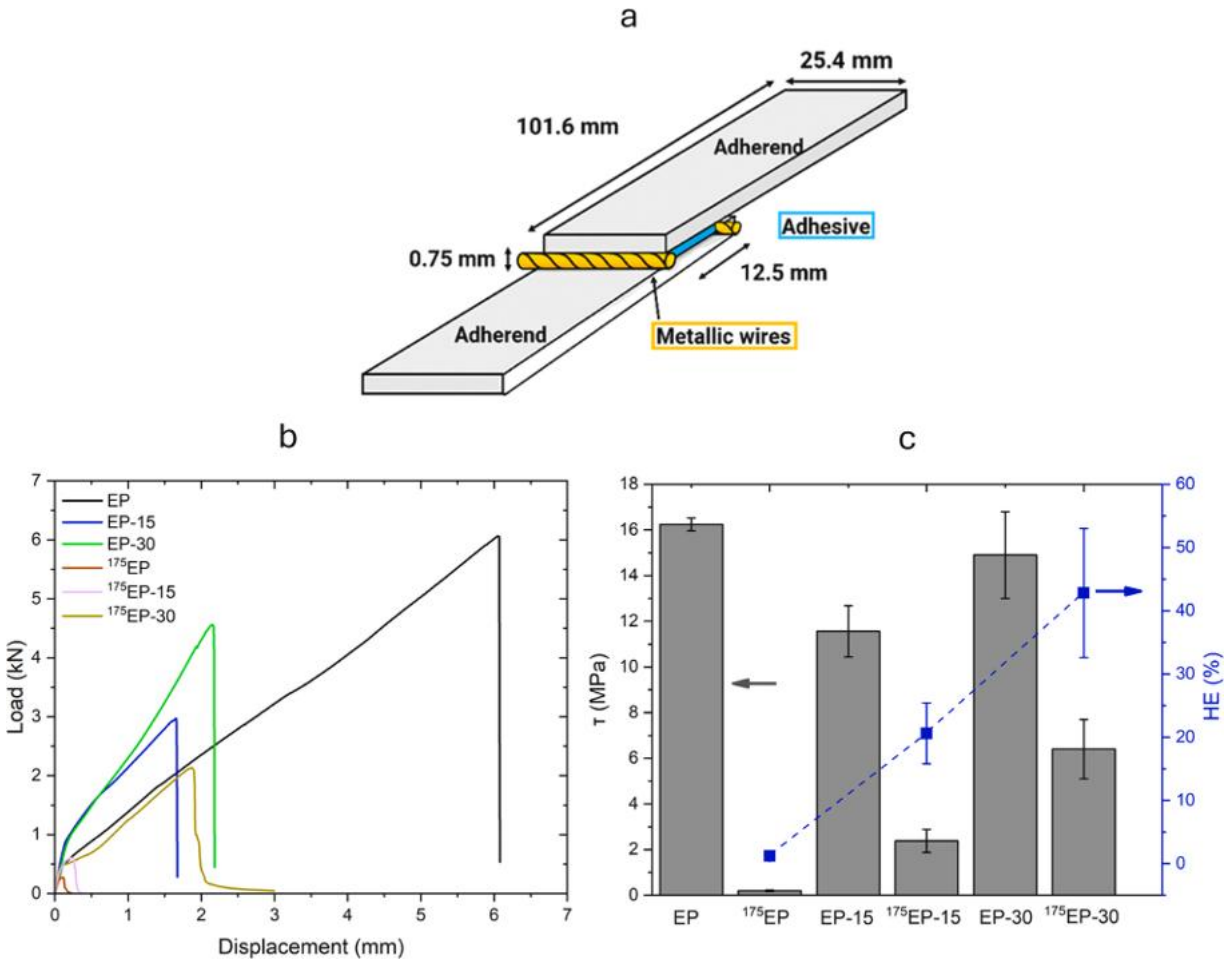


Fig. 3. Single lap shear joint geometry (a), characteristic load-displacement curves for the various adhesive cases (b) and measured lap shear strength and self-healing efficiency (HE) (c).

normal and shear directions (σ_{max}), considered to be equal to each other, and the fracture energy (G_c). Mixed-mode behavior is not considered. The Mode II and III fracture energies are considered to be equal to that for Mode I. The stiffness for all directions is set to 10^6 MPa/mm.

3.3. Modeling healing and residual thermal stresses of the blends

Now, the healing process of the blends is modeled. Complete healing is considered first, where all the elements within the crack region are filled with COC. Therefore, the elements of the crack which initially contained epoxy adhesive material, now contain COC material at a cross section at the middle of the RVE domain, as in Fig. 6. This is based on observations of the healed microstructure of EP/COC blends from Ref. [6]. Approximately one global element size was used as the thickness of the healed region. A case where a few regions are not completely healed or have lost their adhesion is also considered, to study the effect of partial healing. The sizes and locations of the non-healed regions of the crack face are chosen randomly.

To simulate the thermal stresses that are developed during the healing process, a non-linear, transient coupled thermal-displacement analysis in ABAQUS is used. The thermal properties for the COC as measured in the experiments (Table 1 and Table 2) are used, and the properties from Sun and Mishnaevsky Jr. [23] are considered for EP. For the healing process, the applied temperature profile rises from 20 °C to 175 °C within 15 min, then the temperature of 175 °C is kept constant for 1 h, and finally the temperature drops back to 20 °C in 15 min.

However, when the temperature exceeds the glass transition temperature T_g for both EP and COC, the thermal expansion coefficient can increase dramatically, and the Young's modulus can decrease by orders of magnitude. Therefore, the properties of Table 1 and Table 2 are not expected to fully capture the behavior of COC at the healing temperatures of 145 °C and 175 °C, which are well above its T_g (around 80 °C for EP). For this reason, an additional study is performed, where the change of Young's modulus and coefficient of linear thermal expansion (CLTE) are modelled according to the conceptual diagrams of Fig. 6a,b. For COC, the stiffness begins to drop linearly starting from T_g-10 °C, falling to 8 MPa at $T_g + 10$ °C and remains at that value for larger temperatures. For the CLTE, the values of Table 1 are linearly interpolated in the range −30 to 55 °C, then the CLTE remains constant at $0.9{\cdot}10^{-4}$ K^{-1} up to T_g-10 °C and then rises linearly to a double value of $1.8{\cdot}10^{-4}$ K^{-1} at $T_g + 10$ °C. Its value hen remains constant for larger temperatures. A doubling of the CLTE above the glass transition temperature is common for many polymers. For EP, a value of T_g equal to 70 °C is used, according to Truschelli et al. [4]. The CLTE for EP rises from $5.44{\cdot}10^{-5}$ K^{-1} at the glassy state to $1.8{\cdot}10^{-4}$ K^{-1} at the rubbery state. The stiffness of EP is considered unchanged in the rubbery state, which is worst case scenario as the large expansion due to the increase in CLTE together with high stiffness is expected to generate larger residual plastic strains in EP. These values are not the true measured values of EP and COC, but they serve the purpose of a what-if analysis accounting for the effects of glass transition. During the heating process, periodic boundary conditions continue to apply. The load is applied along the Z direction and is perpendicular to the healed crack face.

In this study, stiffness changes due to changes in temperature are accounted for using a table-lookup approach, without directly using a

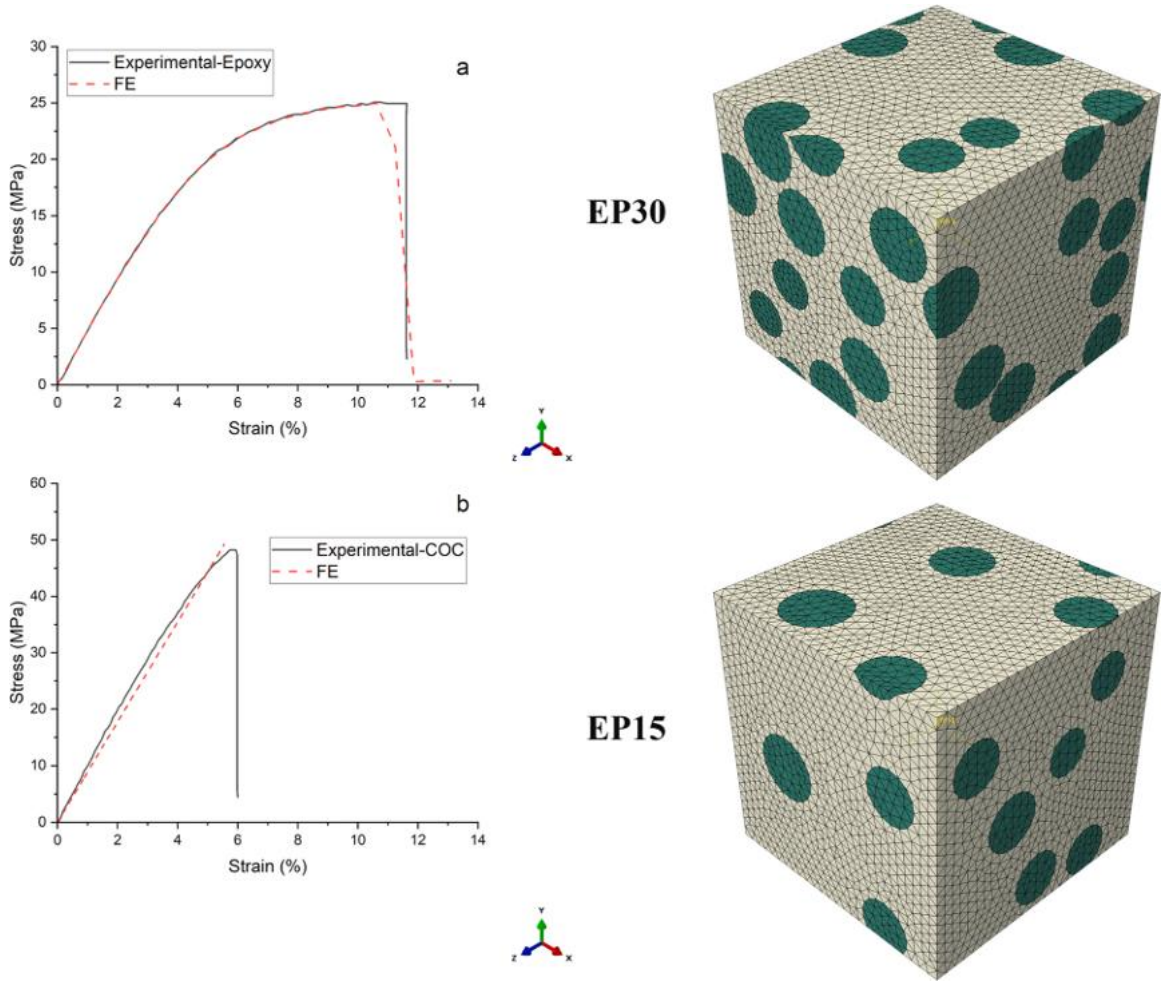


Fig. 4. Comparison between experimental and FE simulation tensile curves for EP (a) and COC (b), and illustration of the RVE's of the EP30 and EP 15 blends used in the FE simulations. COC particles: green color, EP: beige color.

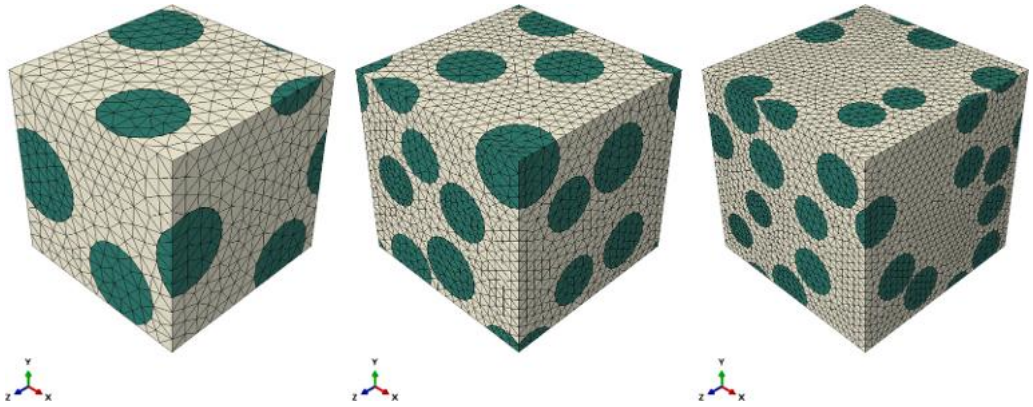


Fig. 5. RVE models of EP30 for the RVE size sensitivity study. The chosen sizes are 0.5 mm (left), 0.75 mm (middle) and 1 mm (right).

viscoelastic model. In this way, only stiffness change is considered and not time-dependent relaxation phenomena. In fact, this kind of approach is particularly suitable whenever monotonic loading conditions are considered with no need to model loading-unloading cycles: in this case there is no need to track historical state variables or manage path-dependent hysteresis branches. However, the developed model could easily be expanded to include a viscoelastic model if experimental stress relaxation data for the different materials were available.

After the heating process is complete, thermal residual stresses are formed within the RVE. Subsequently, the healed model is loaded using the static, non-linear implicit solver in ABAQUS, by applying tensile displacement at the right edge. In the thermal healing simulations, the damage modules are activated only during the cooling process, when the temperature falls below T_g. In the case of the partially healed crack face, the thermal analysis prior to uniaxial loading is not considered, and only the mechanical loading phase is simulated. For the coupled thermal-displacement simulations, 4-node thermally coupled tetrahedron, linear displacement and temperature elements (C3D4T) are used.

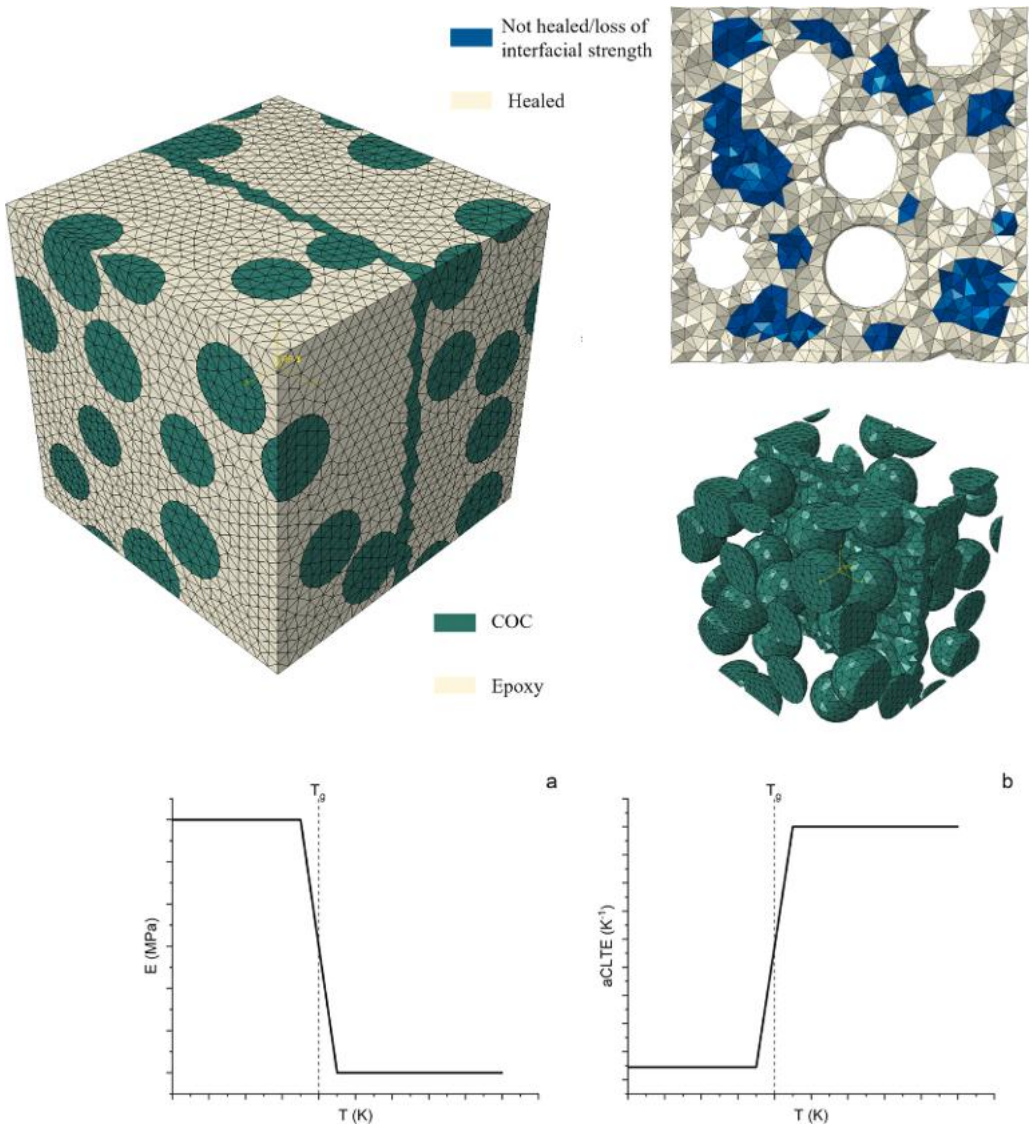


Fig. 6. Illustration of the modelling of the healing process by filling cracked elements with COC. A crack in the center of the RVE domain is considered. A cross section of the COC material in the crack faces is shown in the top right, along with regions that are not filled with COC/lost interfacial adhesion. Schematic of the modelled change in stiffness (a) and Coefficient of Linear Thermal Expansion (CLTE) (b) due to temperature increase above the glass transition temperature T_g.

Due to the thermal properties of the polymers above the glass transition temperature not being available from experimental measurements, only a what-if analysis using estimated values could be performed. The main purpose is to showcase the capabilities of the developed computational model, which could easily incorporate precise thermal properties if they were experimentally measured. The purely what-if analysis is still useful for exploring how thermal properties can affect the post-healing performance.

3.4. Mode I strain energy release rate considering partial healing

Finite element simulations are now performed to calculate the mode I fracture energy of the virgin polymer blends EP30 and EP15, as well as the fracture energy of the healed blends. To do that, the SENB specimen which was used to obtain the experimental G_{IC} values is modeled. The finite element model is shown in Fig. 7. At the tip of the crack, a square RVE of the blend microstructure, with a side length of 1 mm is placed, following a hierarchical modelling approach [48]. The two supports are modelled by constraining the displacement along the Y axis for two nodes on the bottom edge of the model. The distance between the nodes is 40 mm. The load is modelled by a displacement boundary condition at the node which is located at the middle of the top edge. The node is only allowed to move downwards and the applied load at this node is monitored during the analysis to construct the load-displacement curves.

A combination of two dimensional linear triangular and quadrilateral plain strain elements with one integration point (CPE3 and CPE4R) and a 5 mm section thickness are used, both for the crack tip RVE and the surrounding material. A global size of 0.02 mm is used inside the crack tip RVE. The model is solved using a quasistatic explicit solver approach to handle large non-nonlinearities. While a 3D RVE version would be more representative, the 2D models are still useful for understanding the effect of imperfect crack filling. The main goal is to demonstrate the approach, and the same approach could be used with the 3D RVE model at the crack tip.

For the Young's modulus, $E = 640$ Mpa for EP30 and $E = 600$ Mpa for EP15, which is calculated from the numerical stress-strain curves of the RVE models for tension loads (Fig. 10), for a strain level up to 1%. For the Poisson's ratio, $\nu = 0.42$ is used, from the experimental measurements for both EP30 and EP15. The same values are used for the surrounding material in the healed configurations, since damage will be confined near the crack tip area and no change in the response of the

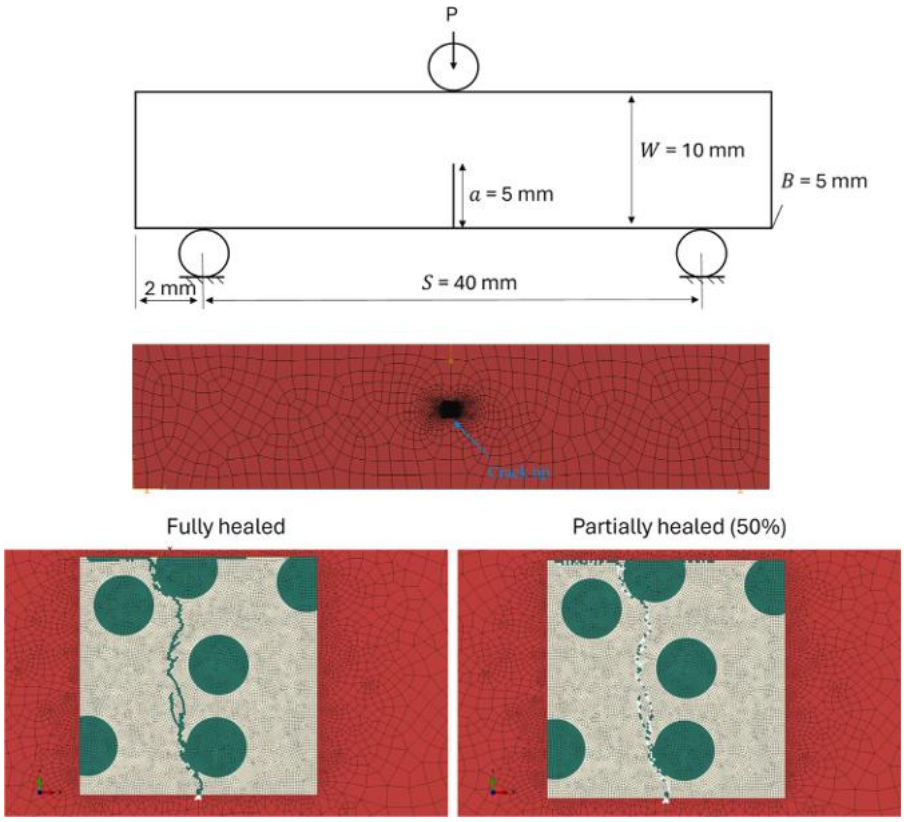


Fig. 7. Dimensions and FE model of the SENB specimen and illustration of the fully and partially healed models for one of the EP30 microstructures.

surrounding material is expected. As the model is loaded, damage initiates and element failure occurs within the crack tip RVE, and the crack begins to propagate. For COC in this case, a linear elastic material with exponential damage is used with stiffness degradation after a critical strain value has been achieved. The damage variable D for COC is calculated with Eq. (5).

$$D = 1 - \frac{\varepsilon_0}{\varepsilon_{\max}} \exp\left(-\frac{E\varepsilon_0 L_c}{G_f} (\varepsilon_{\max} - \varepsilon_0) \right) \tag{5}$$

Where ε_0 is the critical strain value for damage initiation, $\varepsilon_{\max}$ is the maximum principal strain achieved during the loading process, E is the Young's modulus, and L_c and G_f are the characteristic element length and fracture energy, respectively. For COC, the elastic constants E = 886.1 Mpa and $\nu = 0.4$, and fracture energy $G_f = 200$ J/m^2 are used. The value of ε_0 is calculated as $\varepsilon_0 = S_{\max}/E$, where $S_{\max}$= 49.2 Mpa is the tensile strength of COC.

Three RVE geometries for the virgin EP30 and EP15 are examined, and the same geometries are examined after healing has taken place for EP30.

To calculate G_{IC}, Eq. (6) is used:

$$G_{IC} = \frac{Pu}{2WB\varphi} \tag{6}$$

where P is the applied load, u is the displacement of the loaded node, W = 10 mm is the width of the SENB specimen, $B = 5$ mm is the thickness of the SENB specimen and $\varphi = 0.246$ from the ASTM D5045 standard. The values of P and u used in the equation correspond to the maximum load and corresponding displacement at the point of element failure and crack initiation in the models.

For the healed geometries, full crack healing is considered, where all cracked elements of the virgin material simulation are filled with COC, and also imperfect healing where only half of the cracked elements are filled with COC. The elements which are filled with COC are chosen randomly. The Crack patterns for one of the considered geometries for EP30, along with the fully healed and partially healed crack models are also shown in Fig. 7.

3.5. Modeling the behavior of the single lap shear joint

For modeling the SLS joint under quasistatic load, 2D FE models are constructed in ABAQUS 2023, as shown in Fig. 8. Plain strain conditions are applied for the adherends through the use of reduced integration, 4-node bilinear plane strain quadrilateral (CPE4R) elements. The adhesive region is modelled using linear 4-node two-dimensional cohesive elements (COH2D4). One end of the SLS joint is clamped and the other is loaded in tension.

A cohesive zone model is used for the behavior of the adhesive under combined normal and shear loads, which are commonly present in the adhesive in SLS joints. The adhesives of this study generally exhibit high plastic strains. For this reason, a mixed-mode cohesive traction-separation model is used, based on a study by Yang and Thouless [49]. Yang and Thouless [49] used a trapezoidal traction separation law

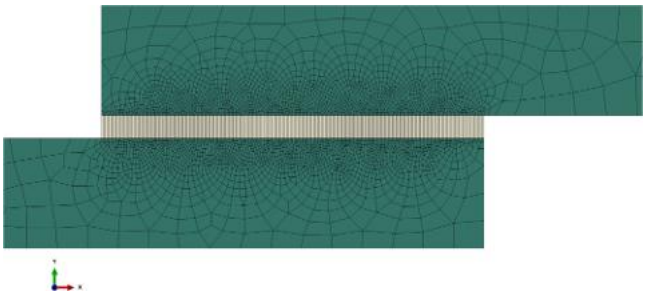


Fig. 8. FE model of the SLS joint showing the overlap region and the adhesive between the two adherends.

both for Mode I and Mode II loading. In this study, a traction separation law of the form shown in Fig. 9 is used for pure Mode I and Mode II loads. This form of traction separation law can accurately capture the load-displacement behavior of the SLS joints, as will be shown in the results section.

Normal tractions are denoted as σ, shear tractions as τ, normal separations as δ^n and shear separations as δ^s. The traction-separation law for Mode I consists of three linear segments. The first linear segment end s at the point (σ_1, δ_1^n), the second linear segment ends at the point (σ_2, δ_2^n), and no further traction can be carried beyond a separation value of δ_f^n. The equivalent values for Mode II tractions are τ_1, τ_2 and equivalent values for Mode II separations are δ_1^s, δ_2^s and δ_f^s. The total area under the Mode I traction separation law is equal to the Mode I critical strain energy release rate G_{IC} and the total area under the Mode II traction separation law is equal to the Mode II critical strain energy release rate G_{IIC}. Generally, for structural adhesives G_{IIC} is considerably larger than G_{IC} [50,51].

As in the study by Yang and Thouless [49], the Mode I and Mode II energy release rates (G_I and G_{II}, respectively) are computed independently, based on the current normal and shear separation values. A failure criterion is then used, given by Eq. (7):

$$\frac{G_I}{G_{IC}} + \frac{G_{II}}{G_{IIC}} = 1 \tag{7}$$

The stiffness of the first linear segment is E_n and E_s for normal and shear loads, respectively. For both of these values, a penalty stiffness of 10^5 Mpa/mm is used, and therefore the separations δ_1^n and δ_1^s can be computed as σ_1/E_n and τ_1/E_s, respectively. This reduces the number of input parameters to σ_1, σ_2, δ_2^n, δ_f^n, τ_1, τ_2, δ_2^s and δ_f^s. A further reduction of input parameters can be achieved by realizing that most of the energy dissipation occurs up to the separation values of δ_2^n and δ_2^s, for both Mode I and Mode II. Therefore, small increases of δ_f^n and δ_f^s, with respect to δ_2^n and δ_2^s, respectively, can be used without affecting the results. An increase of 5% of the δ_2^n and δ_2^s are used for these two parameters, and this reduces the required inputs to σ_1, σ_2, δ_2^n, τ_1, τ_2 and δ_2^s.

The FE model is solved with an explicit solver, to handle large nonlinearities and damage propagation. A quasistatic loading is achieved by keeping the total kinetic energy of the model to less than 5% of the total internal energy. The cohesive traction-separation law is implemented via a VUMAT subroutine. 200 cohesive elements in the overlap region were found to be sufficient to produce mesh independent results. In Section 4.4, the values of σ_1, σ_2, δ_2^n, τ_1, τ_2 and δ_2^s are varied to observe how they affect the load-displacement response of the SLS joint and qualitative relationships between their values and the various virgin and healed adhesives are drawn.

For simplicity and due to lack of experimental data, the CFRP adherends are modelled as a linear elastic material. The stiffness E is determined by a parametric study, so that the initial stiffness of the SLS joint matches the experimental load-displacement curves.

A nonlinear coupling of the two loading modes might be used as well and might be able to better describe the joint behavior. However, in this study, the simplest approach of linear mode coupling is used, and its accuracy will be examined through comparison with the experimental load-displacement curves of the joints.

4. Results

4.1. Tensile performance of the virgin material blends

The resulting tensile curves from the simulations are presented in Fig. 10a,b, for three RVE's with different microstructures, both for EP30 and EP15 (EP30-1,2,3 and EP15-1,2,3). The point of crack initiation and propagation within the RVE corresponds to the point where stress begins to decrease in the curves. The state of the RVE model at the time when the applied load begins to rapidly decrease is also presented in Fig. 10. The computational time for the RVE models was about 1 h (Intel Xeon E5-2640 v3, 2.60 GHz, 16 CPUs)

The experimental curves of the virgin EP30 and EP15 curves are also plotted in Fig. 10. We observe that the RVE models provide an accurate prediction for the value of the maximum stress and the point of failure. Differences are observed in the simulation curves between the three EP15 and EP30 models, which is due to the different microstructures. The stiffness of the stress-strain curve is generally captured accurately, more so for the EP30 models. The maximum strain at failure is higher in the simulations than the experimental curves, indicating that failure might initiate at the interface between EP and COC and that the interface strength might be lower than the EP and COC bulk strengths.

The predicted maximum stress and strains at failure are presented in Table 3 and are compared to the experimental results. The predicted values are close to the experimentally measured values, validating the RVE models. The percentage error using the average values and the root mean square error (RMSE) using all three simulated datapoints and the average experimental strength are presented in Table 4.

A mesh sensitivity study is also performed to verify that the global mesh size of 40 μm produces converged results. Three global mesh sizes are examined (20 μm, 30 μm and 40 μm) for the case of EP30-1. The results are presented in Fig. 11 and it is observed that the global size of 40 μm produces converged results.

The results of the RVE size effect analysis are presented in Fig. 12 for the strength and strain at failure. It is observed that the sizes of 0.75 mm and 1 mm provide results that differ very little from another, and therefore a size of 1 mm is descriptive of the macroscopic behavior of the blends.

Fig. 13 presents the simulated values of damage in the microstructure of EP15-1 at two locations right before the point of failure. Damage in EP is predicted to accumulate at the interface of EP/COC while damage also occurs inside the COC particles with a significant number of cracked COC elements (STATUS=0). The blend eventually fails when damage values in EP reach high values close to one.

Fig. 14 shows the effect of different interface damage parameters on the simulated response for the EP30-1 RVE model compared to the case

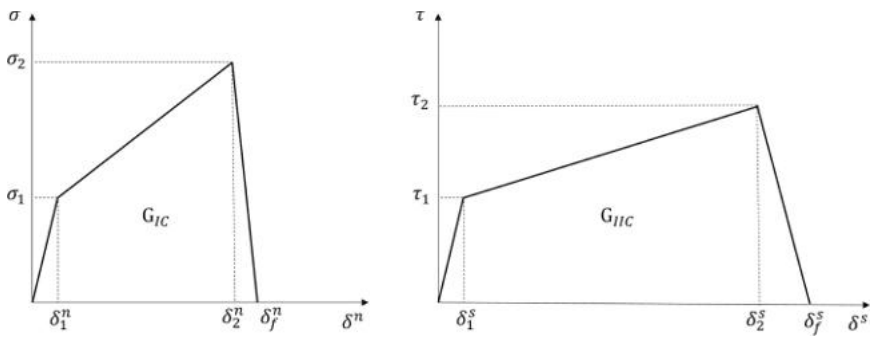


Fig. 9. Traction separation laws for Mode I and Mode II loading, used for the adhesive in the FE models of the SLS joint.

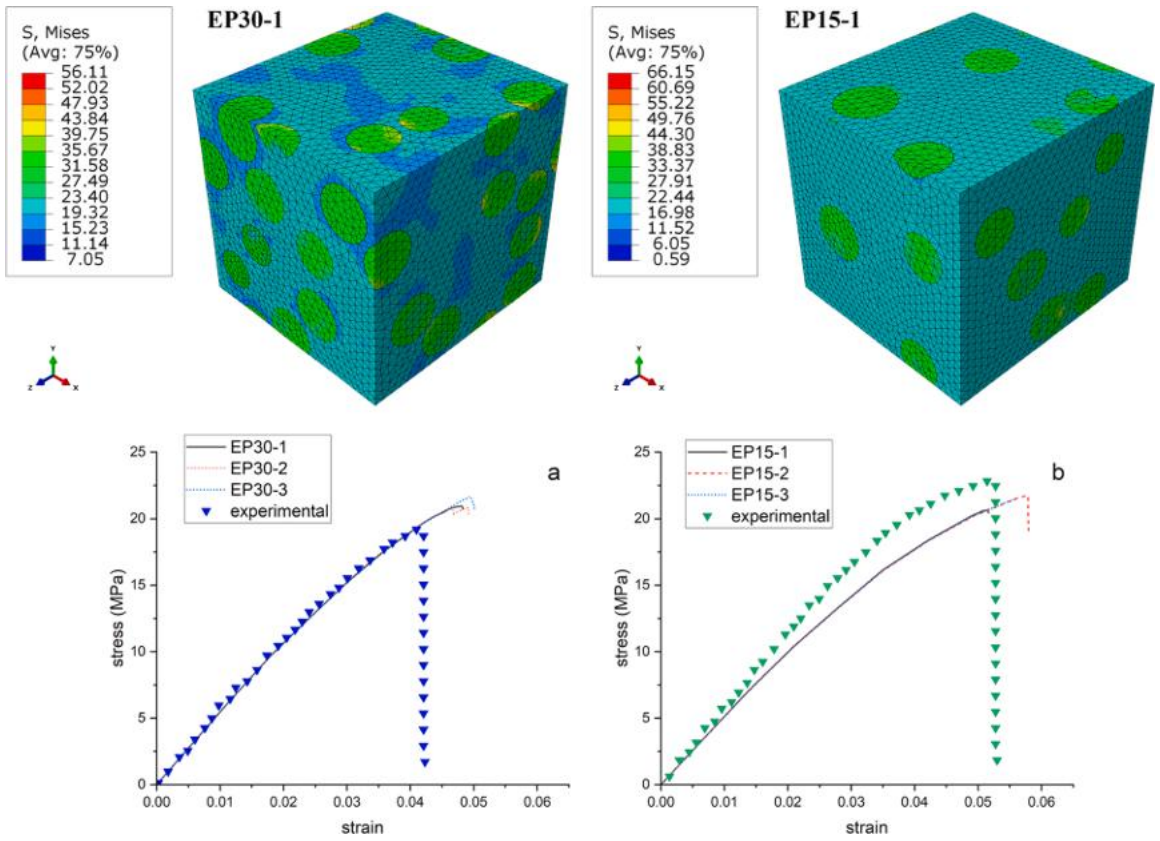


Fig. 10. Comparison between the experimental tensile curves of the EP30 (a) and EP15 (b) blends and those obtained by three RVE models. The state of the RVE model at the time when the applied load begins to rapidly decrease are also presented in the top images. Values of stress in the contours are in Mpa.

Table 3
Experimental and model predicted strengths and strains at failure for the EP15 and EP30 blends.

Blend	σ_{max} [Mpa] experimental	σ_{max} [Mpa] model	ε_{fail} [%] experimental	ε_{fail} [%] model
EP15	24.0 ± 0.8	21.3 ± 0.6	5.40 ± 0.57	5.53 ± 0.31
EP30	20.5 ± 0.8	21.2 ± 0.5	4.20 ± 0.25	4.90 ± 0.10

Table 4
Error metrics between experimental and simulated strengths and failure strains.

Metric	EP30		EP15	
	σ_{max}	ε_{fail}	σ_{max}	ε_{fail}
Percentage Error (%)	3.25	16.67	11.11	2.47
RMSE	0.39	0.08	0.46	0.25

where no interface damage is modelled. Given that the no interface damage case closely matches the experimental curve, the model suggests that the interface peak stress before damage initiation is around 45 MPa, which is higher than the peak stress of EP but lower than that of COC. This indicates that the interface strength value is somewhere in-between the strength of EP and COC.

4.2. Effect of healing and thermal residual stresses on tensile performance

The thermal residual stresses were predicted using the coupled temperature-displacement simulations, considering the effects of glass transition at elevated temperatures, according to the approach described

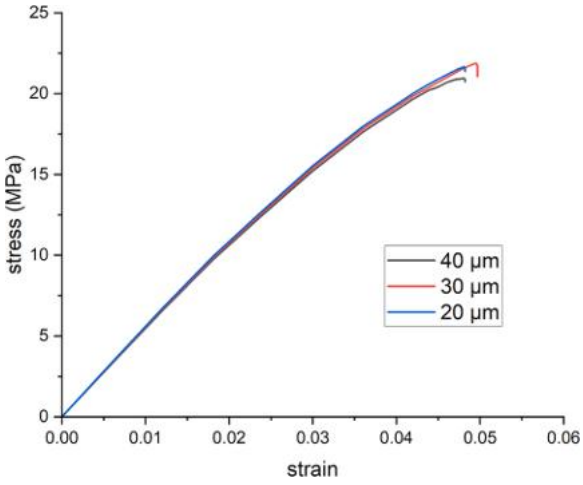


Fig. 11. Mesh sensitivity study for the RVE model for EP30-1, using three different global mesh sizes.

in Section 3.3. In Fig. 15a, the von Mises residual thermal stresses at the end of the healing process (at 175 °C) are presented for one of the fully healed EP30 models. The residual stress values generally low and in the range of 0.1 MPa. In Fig. 15a, the state of the RVE simulation at the point where stress begins to rapidly drop is presented.

After healing, the EP30 RVE is loaded in tension and the resulting stress strain curves up to the point of failure are presented in Fig. 16. The performance of the virgin material from Section 4.1 is also plotted for comparison. The tensile response corresponding to partially healed crack is also plotted. The curves are plotted up to the point where crack

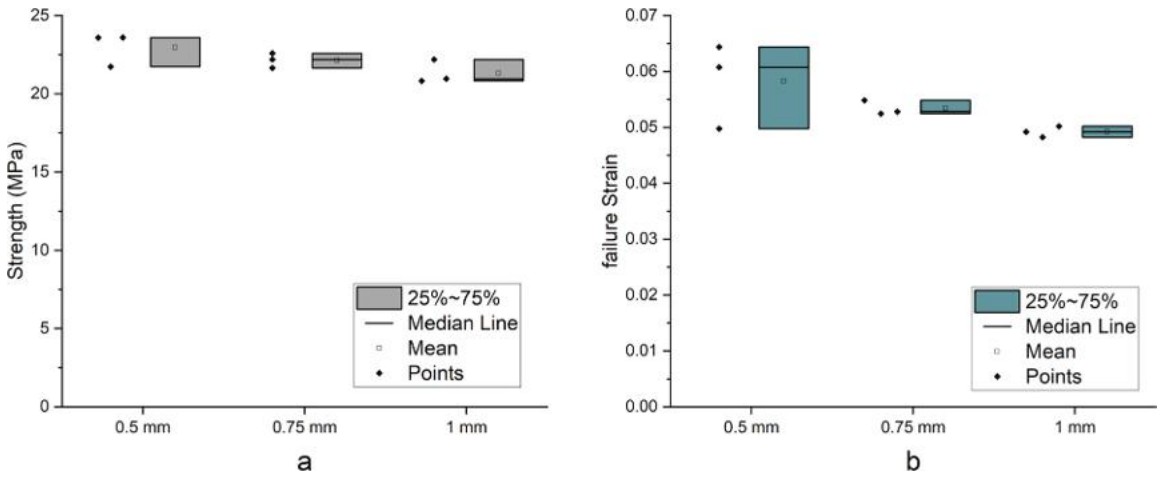


Fig. 12. Results of the RVE size sensitivity analysis for the macroscopic (a) strength and (b) failure strain of the EP30 blend.

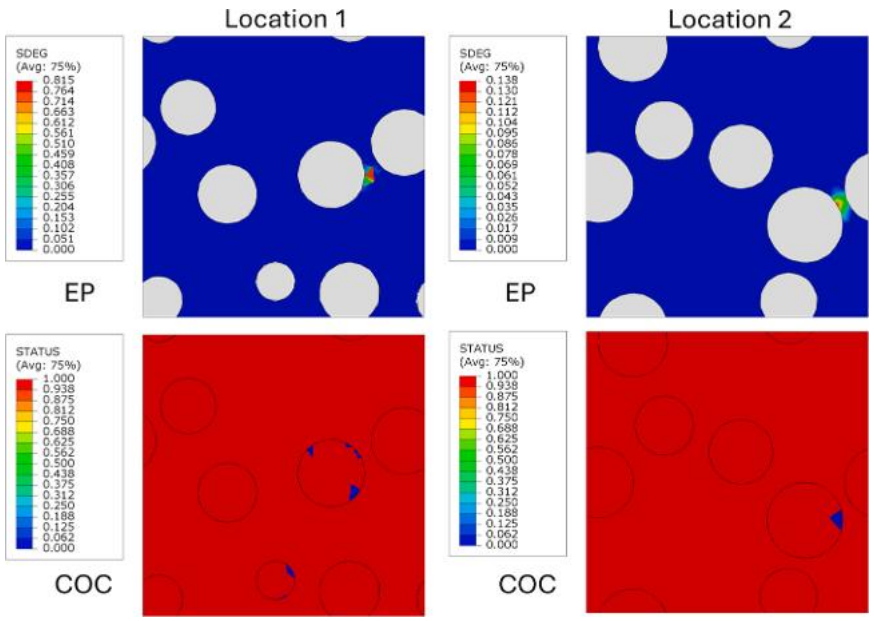


Fig. 13. Damage values in the microstructure of one of the EP15 blends at two locations right before blend failure. The damage variables are shown for EP (SDEG) and the number of cracked COC elements (STATUS=0) is also presented.

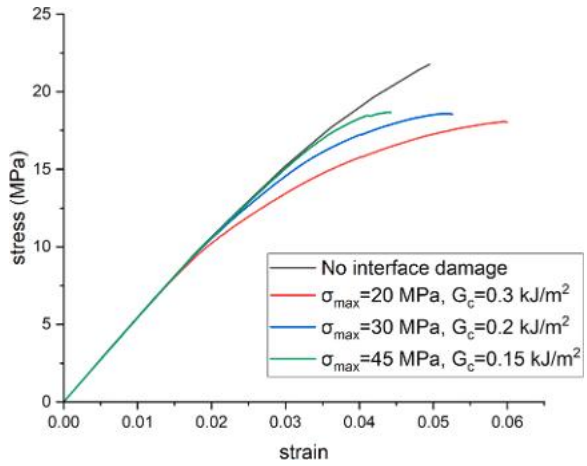


Fig. 14. Effect of interface cohesive law damage properties on the simulated response of the EP30-1 RVE model.

initiation occurs and the stress begins to drop rapidly.

The performance of the healed material, considering thermal residual stresses with glass transition effects is predicted to be superior to that of the virgin material. This indicates that the healed material, in case of perfect healing could potentially fully restore the load carrying capacity. This superior performance compared to the virgin material might be an indication that the worse performance of the healed adhesives in the SLS test, as observed experimentally, is dependent on other mechanisms, such as incomplete or imperfect healing of the crack region. The tensile curves for partially healed crack faces predict a performance reduction, where the strength is lower than that of the virgin material.

4.3. Prediction of mode I fracture energy of the virgin and healed blends

As the SENB FE model is loaded, crack initiation and propagation occurs at a certain load value. The resulting load-displacement curves for the three crack tip RVE's of the virgin EP30 and EP15 blends, and also for the fully and partially healed EP30 cases are presented in Fig. 17a,b. A model that contains only virgin EP is simulated to construct the corresponding load displacement curve in Fig. 17 for comparison

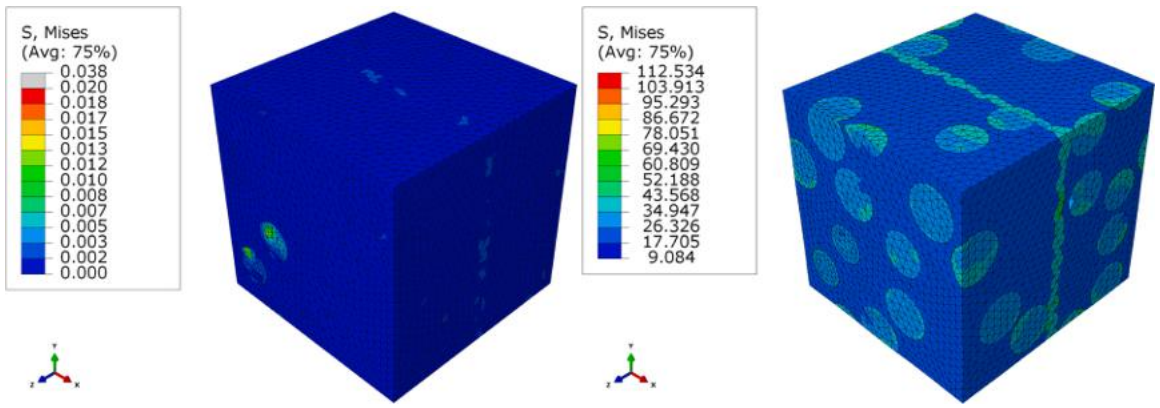


Fig. 15. (a) Residual stress distribution at the end of the healing process for model 1 of EP30 blends. 175 °C healing temperature.(b) state of the RVE at the point where stress begins to drop rapidly. Values of von Mises stress in MPa.

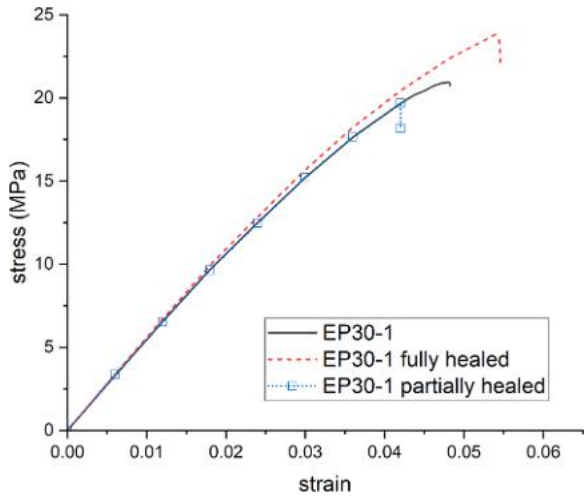


Fig. 16. Simulated stress-strain curves of the virgin and healed blends for EP30 (a) and EP15(b), without considering glass transition effects for the healed cases. The resulting curves without considering residual thermal stresses formed during the healing process, and with consideration of partial healing of the crack faces are also plotted for comparison. A close-up of the rectangular region is presented on the right of each graph. Tensile stress-strain curves of the virgin and healed at 175 °C material, with consideration for glass transition effects during the healing process, for EP30 (c) and EP15 (d).

purposes. The load value used in the G_{Ic} calculations is determined as the load for which at least three or more elements have failed near the crack tip. The computational time for the SENB models was about 30 min (Intel Xeon E5-2640 v3, 2.60 GHz, 16 CPUs)

The average G_{IC} values of the three different RVE geometries for each case, calculated using Eq. (6), are presented in Fig. 17c. The results for full and partial/imperfect healing are also presented in Fig. 17d. A good prediction of the Mode I fracture energy, G_{IC}, is achieved for the virgin EP30 and EP15 blends, and also for the virgin EP. The models predict the same trend of G_{IC} values as the experimental results, with EP having a greater G_{Ic} than EP30 and EP30 having a greater G_{IC} value than EP15. The prediction of G_{IC} considering full healing of the crack faces is nearly identical to that of the virgin material. The fracture energy value is reduced significantly when considering partial healing of the crack faces.

This result indicates that partial healing of the crack faces may be another reason for the performance degradation of the healed blends in the fracture toughness tests and also in the single lap shear joint tests. The viscosity of the COC decreases as the temperature increases, and this helps the healing material to flow in-between the crack faces. Therefore, a larger portion of the crack could be filled with COC material at the healing temperature of 175 °C than at 145 °C, and this could be the reason for the lower fracture toughness of the healed EP30 blend at 145 °C in the experiments.

The effect of crack face filling percentage with COC is also examined. Models with various filling percentages are simulated and the resulting G_{IC} value is plotted as a function of crack filling percentage in Fig. 18, for the case of EP30M1.

The value of G_{IC} is predicted to increase with increasing crack filling percentage, but with the rate of increase slowing down and reaching a plateau after a filling percentage of 75%. A sigmoid-like relationship appears to exist, according to the simulation results.

4.4. Modeling the behavior of the single lap shear joint

The results of the SLS FE models are presented in Fig. 19, for various values of the traction-separation law parameters (σ_1, σ_2, δ_2^n, τ_1, τ_2 and δ_2^s) and compared to the experimental load-displacement curves for the virgin EP, virgin EP30, and healed ^{175}EP30 adhesives. The Young's modulus for the CFRP adherends was determined to be equal to E= 20 GPa and Poisson's ration ν= 0.33, to match the initial stiffness of the SLS load-displacement curves. The computational time for the SLS models was about 15 min (Intel Xeon E5-2640 v3, 2.60 GHz, 16 CPUs).

For the parameters related to Mode I, the values of σ_1, σ_2, δ_2^n are chosen so that a similar value to the experimentally measured G_{IC} is obtained for all different adhesives. The value of σ_2 is considered equal to the peak stress of the tensile stress-strain curve of each adhesive. The value of σ_1 can be considered equivalent to the yield stress, which has a low value for the considered adhesives. There is a lot of shear involved in the SLS joint, and therefore the Mode II parameters are expected to have the biggest influence on the results.

From the numerical curves, a few observations can be made. First, the separation value δ_2^s controls the maximum displacement of the joint for which failure occurs. Also, the peak shear traction τ_2 controls the peak force of the force-displacement curve. The combination of τ_2 and δ_2^s controls the stiffness of the second "linear" part of the load-displacement curves. This verifies the big influence of the Mode II load in the response of the joint. Furthermore, the values of σ_1 and τ_1 control the length of the first "linear" part of the load-displacement curves and signal yielding.

A mesh size sensitivity study for the SLS models is also performed, using three different mesh densities for the adhesive layer (50, 100 and 200 elements). The results are presented in Fig. 20, along with the cohesive zone model parameters used in the mesh sensitivity analysis.

The comparison of the numerical curves to the experimental data suggests that the inclusion of COC particles generally raises the yield point of the first "linear" segment of the SLS load-displacement curve, while reduces peak Mode I traction and maximum separation before

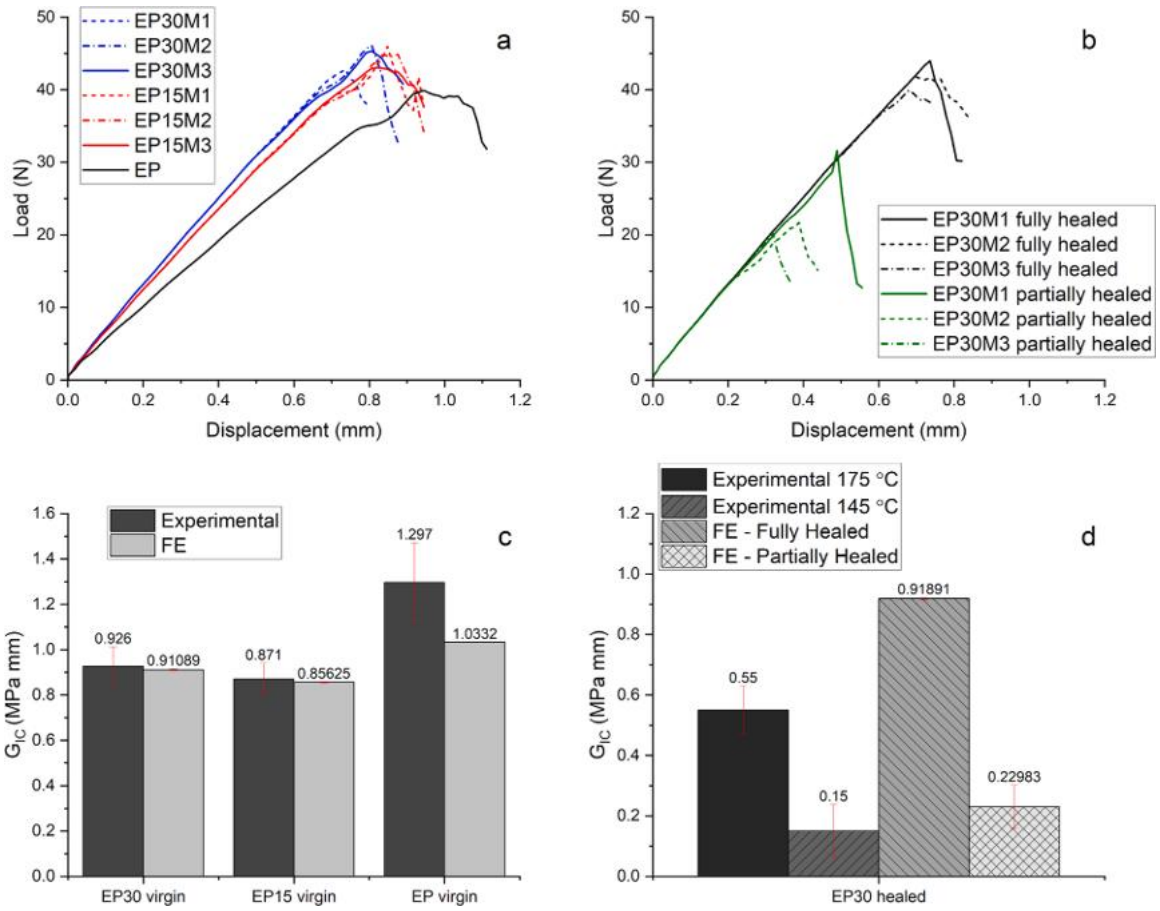


Fig. 17. Load-displacement curves for the three crack tip RVE's of the virgin EP30 and EP15 blends (a) (the results for virgin EP are also included), and also for the fully and partially healed EP30 (b). The points of crack initiation, which are used to calculate G_{Ic} are also plotted. Average fracture toughness values of the FE models compared to the experimental values, for the virgin EP30 and EP15 blends (c), and for the healed EP30 at 175 ^{0}C and 145 ^{0}C considering full and partial healing of the crack faces (d).

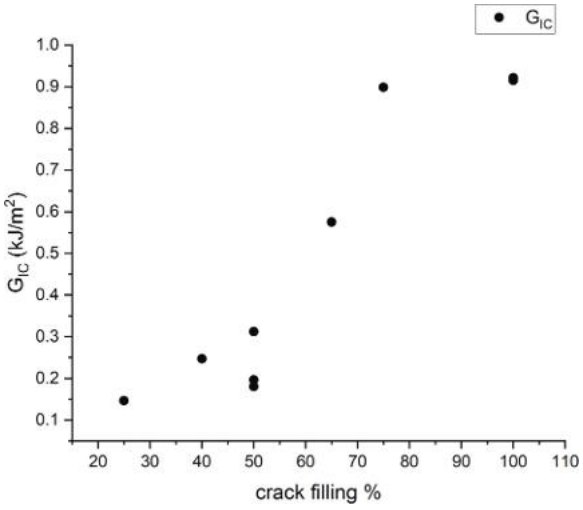


Fig. 18. Simulated G_{IC} value as a function of crack face filling percentage with COC, for EP30M1.

failure (δ_2^s), compared to the virgin EP. The healed EP30 blend exhibits a further reduction of τ_2 and δ_2^s, while the yield point also decreases, suggesting lower σ_1 and τ_1 values than the virgin blend.

The ratio G_{IIC}/G_{IC} can be a performance indicator for these types of adhesives, in addition to the peak traction values. If the ratio is calculated for the numerical curves which best fit the experimental data in Fig. 19 (dash-dot curve in Fig. 19a for EP, solid curve in Fig. 19b for EP30 and dash-double dot curve for ^{175}EP30), then a value of 35.85 is obtained for EP, 17.44 for EP30 and 9.45 for ^{75}EP30. These values are calculated using areas under the traction-separation laws up to δ_2^n and δ_2^s. In the case of EP, the adhesive failure mode in the experiments was found to be adhesive. Therefore, there is additional potential in the adhesive material to reach higher values of joint strength.

From the results of Fig. 19 it is clearly observed that the Mode II peak traction and displacement values have the greatest influence on the results, and that a single pair of τ_2 and δ_2^s will result in a distinct joint failure point each time. The contribution of Mode I is negligible. Given that the Mode I parameters can more easily be measured experimentally and that different pairs of τ_2 and δ_2^s will provide a different peak joint force each time, the existence of dual parameter sets that lead to same behavior is unlikely. The damage value contour in the adhesive layer for the SLJ model of EP30, right before debonding, is presented in Fig. 21. This indicates that the debonding crack will most likely initiate at these locations, as expected. The highest damage values occur at the overlap ends and significant shear deformation is observed.

5. Discussion

5.1. Modelling considerations

The following simplifications in the modelling have been made, which could potentially influence the results; The simplification of COC

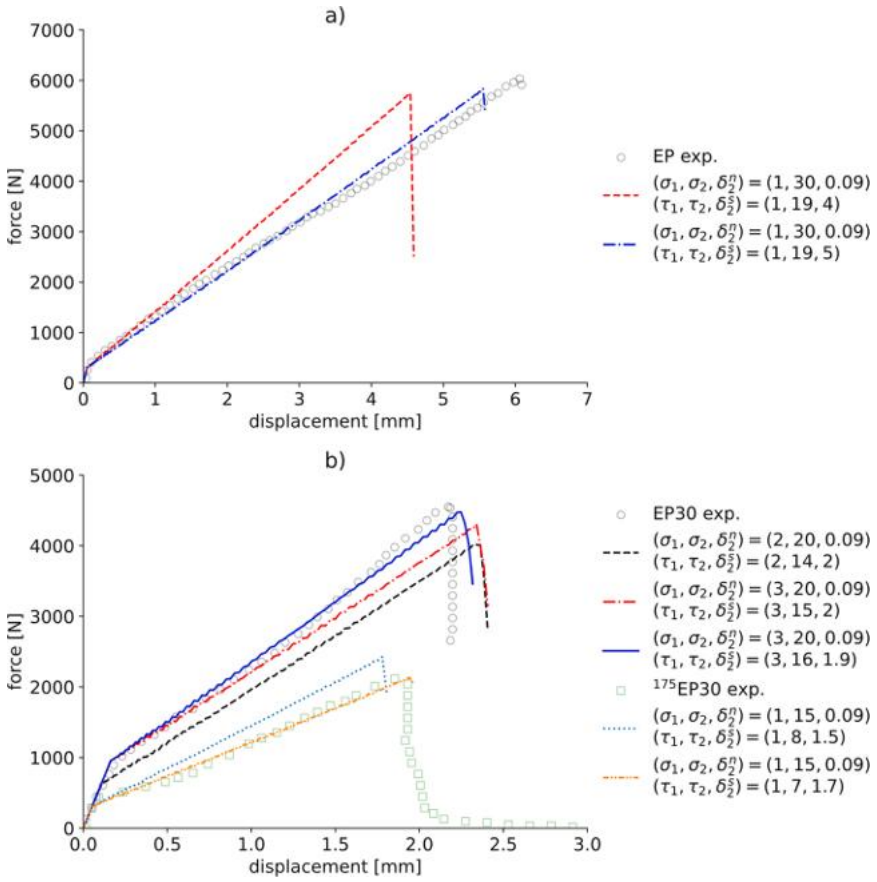


Fig. 19. Experimental and numerical load-displacement curves for the SLS joints, for a) virgin EP and b) virgin EP30 and healed ^{175}EP30. Various cohesive law parameters are used for generating the numerical curves. Values of tractions in MPa and separations in mm.

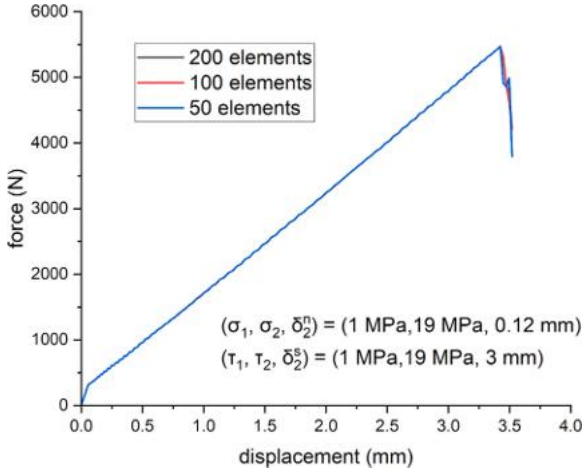


Fig. 20. Mesh sensitivity analysis for the SLS model using three different element densities for the adhesive layer.

particle geometries as spheres may influence the results, as the particles exhibited irregular shapes and a distribution of sizes. The interface between EP and COC was assumed to not be damaged, but an experimental characterization of the interface properties is required to model the interface with higher fidelity. This study examines how well the simplest approximation of COC particles as spheres and perfect interfacial adhesion in the RVE models can provide accurate stress-strain curves. The results with these approximations are quite representative of the experimental results, if one observes Fig. 10. However, both simulated curves predict larger strain at failure than the experimental curves, which indicates that irregular particle shapes and interface failure can lead to earlier fracture.

In this study, the effect of partial or imperfect crack face healing was predicted to significantly reduce the tensile strength and Mode I critical strain energy release rate. However, the percentage of crack face healing was not predicted. In future studies, the amount of filling of the crack faces with the healing agent could be predicted by considering the rheological properties of the healing material, such as its viscosity and its dependence on temperature, and also crack face geometry. Coupling such models that can predict the degree of crack face filling with the models of this study could provide significant predictive capabilities for the healed blends. An approach of using equations developed for porous media flow, such as in the study by Luo et al. [1], could be used to predict the effectiveness of crack face healing and subsequently the healing efficiency.

With the cohesive zone modelling approach adopted in this study, it was not possible to distinguish between cohesive and adhesive failure. For an optimal re-bonding process, it is desired that failure is cohesive, so that the two adherends can be readily brought into contact. This way, healing and re-bonding can be performed without further processing or re-application of the adhesive. Therefore, studies of the parameters that can favor cohesive failure is a promising direction for future work.

Furthermore, the models developed in this study focus on a slow – quasistatic loading rate, using input from stress strain curves obtained for the loading rate of 1 mm/min. For different loading rates, experimental input data obtained at those specific rates should be used in the models.

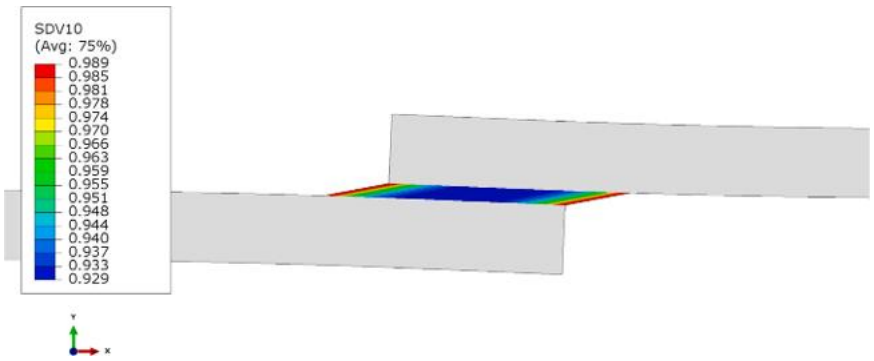


Fig. 21. Damage variable value distribution across the adhesive layer in the SLJ model for EP30, right before debonding.

5.2. Micro-mechanisms that reduce post-healing performance

In this study, partial crack face filling is recognized as a significant cause of performance reduction. This is because it reduced the effective load carrying area and therefore causes failure at lower external stress levels. Imperfect crack face filling is mainly attributed to high viscosity at the healing temperature which prevents some crack face regions to be filled with the thermoplastic phase, or makes it difficult for the thermoplastic phase to flow and fill crack face roughness craters completely, reducing the EP/COC interfacial adhesion strength. At the same time, the thermal treatment needed to reach healing can cause thermal chemical degradation and reduce the cross-linking density of the healed epoxy matrix, leading to reduced stiffness and strength. This can be verified by testing the polymers after repeated healing cycles and observing how the tensile performance after each cycle compares to the initial stress-strain curve. Residual thermal stresses can also cause early damage and loss of interface adhesion between EP/COC phases, but the residual stress values predicted in this study were quite low. Fractography of the separated crack faces of the SENB specimens could provide additional insights on how fracture develops in the blends.

The addition of COC particles seems to reduce the value of G_{IIC} of the adhesive blends, which is most likely due to the load redistribution that the COC particles introduce, reducing the capacity of the adhesive to carry shear loads. In addition, the interfacial strength between COC particles and the epoxy resin is not known and it could be lower than the strength of the bulk polymers. The addition of COC particles may also influence the failure mode of the adhesive joints to occur in the bulk of the blend rather than the blend/adherend interface, changing the failure mode form adhesive to cohesive. Healing appears to further reduce the value of G_{IIC}, most likely due to imperfect damage healing or property degradation of the blends after the thermal healing cycle.

5.3. Cyclic loading and ageing effects

In this study, focus is placed on monotonic quasistatic loading conditions without aging effects. The effects of cyclic loading and ageing are very important for accurate predictions of lifetimes for adhesive joints. These effects can be explored in future studies that examine the effects of multiple healing cycles and ageing on the fatigue lifetime of self-healing adhesive joints. The developed adhesive joint models were able to accurately capture the load-displacement behavior and can be further extended to include fatigue degradation. The thermal residual stress distribution can also change after multiple healing and heating cycles. The flowing and redistribution of COC after each healing cycle could also affect the long term performance of the blends.

6. Conclusions

This study focused on modelling approaches to simulate damage mechanisms in the microstructure of adhesives based on polymer blends with self-healing properties, and to simulate the residual thermal stresses formed during the healing process. The main goal was to study the effect of residual stresses formed during the healing process and partial filling of crack faces by the healing agent on the post-healing performance of the adhesive. RVE models were developed for predicting the tensile strength and Mode I critical strain energy release rate, which are important indicators of the adhesive performance. The models were also used for simulating the healing process in the material microstructure. Coupled temperature-displacement simulations were used for the healing process and particular focus was placed on capturing the effect of property changes due to glass transition of the polymer materials that form the adhesive structure.

The results indicate that the residual stresses formed during healing do not have a negative influence on the tensile strength of the adhesive. On the contrary, partial filling of the crack faces by the healing agent led to significant reduction in both the tensile strength and Mode I critical strain energy release rate of the healed adhesive. The approaches developed in this study can be used to predict the strength and G_{IC} of the virgin material blends to compare against properties of currently used structural adhesives, and to predict how two different polymers in a blend can form residual stresses when heated above their T_g and subsequently cooled to room temperature. However, further analysis and experimental examinations of the failure modes and fracture surfaces of the healed blends are required to identify the exact mechanisms of performance reduction.

Furthermore, the study demonstrated how a multi-linear mixed mode cohesive zone model that accounts for significant plastic deformation in the adhesives was able to capture the response of the SLS joint, in terms of load displacement curves. While cohesive zone modelling is a convenient tool for predicting joint strength, it requires further enhancement to be able to distinguish between adhesive and cohesive failure modes. The latter mode is desired in the case of self-healing adhesives as it allows direct re-bonding of the adherends without further processing. A computational modelling tool that distinguishes between these failure modes would be able to provide design guidelines for ensuring cohesive failure in self-healing adhesive joints.

CRediT authorship contribution statement

Antonios Tempelis: Writing – review & editing, Writing – original draft, Validation, Methodology, Formal analysis, Conceptualization. **Nicolò Truschelli:** Writing – review & editing, Visualization, Validation, Methodology, Formal analysis, Conceptualization. **Laura Simonini:** Writing – review & editing, Validation, Supervision, Methodology, Conceptualization. **Alessandro Pegoretti:** Writing – review & editing, Supervision, Resources, Conceptualization. **Andrea Dorigato:** Writing – review & editing, Validation, Supervision, Resources, Conceptualization. **Leon Mishnaevsky:** Writing – review & editing, Supervision, Resources, Funding acquisition, Conceptualization.

Declaration of Competing Interest

The authors declare that they have no known competing financial interests or personal relationships that could have appeared to influence the work reported in this paper.

Acknowledgements

AT and LM acknowledge the financial support of the Velux Foundation via the project PREMISE "Preventing MIcroplastics pollution in SEa water from offshore wind" (https://premise.dtu.dk/), of the Ministry of Foreign Affairs of Denmark via the Danida Grant 19-M02-DTU "Maintenance and repair strategy for wind energy development" (https://www.maintainergy.dk/), and of the European Commission via Horizon project "Blades2Build: Recycle, repurpose and reuse end-of-life wind blades composites: A coupled pre- and co- processing demonstration plant", Grant agreement 101096437. The authors would like to thank Yulin Chen for her help in the development of the microstructural finite element models.

Data availability

Data will be made available on request.

References

[1] X. Luo, R. Ou, D.E. Eberly, A. Singhal, W. Viratyaporn, P.T. Mather, A thermoplastic/thermoset blend exhibiting thermal mending and reversible adhesion, ACS Appl. Mater. Interfaces 1 (3) (2009) 612–620.
[2] A. Cohades, E. Manfredi, C.J. Plummer, V. Michaud, Thermal mending in immiscible poly (ε-caprolactone)/epoxy blends, Eur. Polym. J. 81 (2016) 114–128.
[3] A. Cohades, V. Michaud, Damage recovery after impact in E-glass reinforced poly (ε-caprolactone)/epoxy blends, Compos. Struct. 180 (2017) 439–447.
[4] N. Truschelli, L. Simonini, A. Tempelis, L. Mishnaevsky Jr, A. Pegoretti, A. Dorigato, Development of self-healing epoxy/COC adhesives for potential use in wind turbine blades, Compos. Part A: Appl. Sci. Manuf. (2026) 109732.
[5] H. Mahmood, A. Dorigato, A. Pegoretti, Thermal mending in novel epoxy/cyclic olefin copolymer blends, Express Polym. Lett. 14 (4) (2020) 368–383.
[6] A. Dorigato, H. Mahmood, A. Pegoretti, Optimization of thermal mending process in epoxy/cyclic olefin copolymer blends, J. Appl. Polym. Sci. 138 (2021) e49937.
[7] L. Simonini, R. Canale, H. Mahmood, A. Dorigato, A. Pegoretti, Multifunctional epoxy/carbon composites with a fully reparable interface, Polym. Compos. 45 (2024) 2558–2568.
[8] M.J. Ramezani, O. Rahmani, H. Ebrahimnezhad-Khaljiri, Experimental investigation of mechanical-healing performance of graphene nanoplate-reinforced microcapsule-based composites under static and dynamic loadings, Polym. Compos. 47 (2) (2026) 1549–1564.
[9] H. Ebrahimnezhad-Khaljiri, R. Eslami-Farsani, S. Mirzamohammadi, Assessment of mechanical and healing behaviors of glass fibers-epoxy composite containing the microcapsules with the nanocomposite shell, J. Appl. Polym. Sci. 140 (1) (2023) e53273.
[10] S. Miao, M.L. Wang, H.L. Schreyer, Constitutive models for healing of materials with application to compaction of crushed rock salt, J. Eng. Mech. 121 (10) (1995) 1122–1129.
[11] E.J. Barbero, F. Greco, P. Lonetti, Continuum damage-healing mechanics with application to self-healing composites, Int. J. Damage Mech. 14 (1) (2005) 51–81.
[12] R.K.A. Al-Rub, M.K. Darabi, D.N. Little, E.A. Masad, A micro-damage healing model that improves prediction of fatigue life in asphalt mixes, Int. J. Eng. Sci. 48 (11) (2010) 966–990.
[13] M.K. Darabi, R.K.A. Al-Rub, D.N. Little, A continuum damage mechanics framework for modeling micro-damage healing, Int. J. Solids Struct. 49 (3–4) (2012) 492–513.
[14] H. Shahsavari, M. Baghani, R. Naghdabadi, S. Sohrabpour, A thermodynamically consistent viscoelastic–viscoplastic constitutive model for self-healing materials, J. Intell. Mater. Syst. Struct. 29 (6) (2018) 1065–1080.
[15] Y. Pan, F. Tian, Z. Zhong, A continuum damage-healing model of healing agents based self-healing materials, Int. J. Damage Mech. 27 (5) (2018) 754–778.
[16] G.Z. Voyiadjis, A. Shojaei, G. Li, A thermodynamic consistent damage and healing model for self healing materials, Int. J. Plast. 27 (7) (2011) 1025–1044.
[17] G.A. Esgandani, A. El-Zein, Thermodynamic based model for coupled elastoplastic damage-healing behaviour of unsaturated geomaterials, Mech. Mater. 145 (2020) 103395.
[18] X. Zhang, P. Zhu, Z. Zhong, A chemo-mechanically coupled continuum damage-healing model for chemical reaction-based self-healing materials, Int. J. Solids Struct. 236 (2022) 111346.
[19] A. Shojaei, G.Z. Voyiadjis, Statistical continuum damage healing mechanics (SCDHM), Int. J. Damage Mech. 32 (6) (2023) 872–885.
[20] B. Ahmed, T. Park, J.S. Jeon, Multi-stress damage and healing mechanics in quasi-brittle materials: Theoretical overview, Int. J. Damage Mech. 34 (6) (2025) 855–877.
[21] H. Subramanian, S.S. Mulay, On the constitutive modelling of elasto-plastic self-healing materials, Int. J. Solids Struct. 234 (2022) 111289.
[22] Z. Dai, X. Zhu, F.A. Gilabert, A multi-material-oriented modeling framework to characterize and predict mechanical self-healing, Int. J. Mech. Sci. 260 (2023) 108644.
[23] Yulin Sun, Leon Mishnaevsky Jr., Healable polymer blends: computational analysis of damage and healing mechanisms, Int. J. Mech. Sci. 287 (2025) 109938, https://doi.org/10.1016/j.ijmecsci.2025.109938.
[24] R. Jahadi, H. Beheshti, M. Heidari-Rarani, A micromechanical damage-healing model for encapsulation-based self-healing polymer composites under tensile loading, Mech. Adv. Mater. Struct. 31 (18) (2024) 4295–4308.
[25] D.S. Dugdale, Yielding of steel sheets containing slits, J. Mech. Phys. Solids 8 (2) (1960) 100–104.
[26] G.I. Barenblatt, The mathematical theory of equilibrium cracks in brittle fracture, Adv. Appl. Mech. 7 (1962) 55–129.
[27] A. Needleman, A continuum model for void nucleation by inclusion debonding, J. Appl. Mech. 54 (3) (1987) 525.
[28] Q.D. Yang, M.D. Thouless, S.M. Ward, Numerical simulations of adhesively-bonded beams failing with extensive plastic deformation, J. Mech. Phys. Solids 47 (6) (1999) 1337–1353.
[29] B.F. Sørensen, E.K. Gamstedt, R.C. Østergaard, S. Goutianos, Micromechanical model of cross-over fibre bridging–prediction of mixed mode bridging laws, Mech. Mater. 40 (4-5) (2008) 220–234.
[30] Z.J. Zhang, G.H. Paulino, Cohesive zone modeling of dynamic failure in homogeneous and functionally graded materials, Int. J. Plast. 21 (6) (2005) 1195–1254.
[31] S. Goutianos, B.F. Sørensen, The application of J integral to measure cohesive laws under large-scale yielding, Eng. Fract. Mech. 155 (2016) 145–165.
[32] K. Tserpes, A. Barroso-Caro, P.A. Carraro, V.C. Beber, I. Floros, W. Gamon, V. Rajčić, A review on failure theories and simulation models for adhesive joints, J. Adhes. 98 (12) (2022) 1855–1915.
[33] Maiti, S., Shankar, C., Geubelle, P.H., Kieffer, J., Continuum and molecular-level modeling of fatigue crack retardation in self-healing polymers, 2006.
[34] A.A. Alsheghri, R.K.A. Al-Rub, Thermodynamic-based cohesive zone healing model for self-healing materials, Mech. Res. Commun. 70 (2015) 102–113.
[35] A.A. Alsheghri, R.K.A. Al-Rub, Finite element implementation and application of a cohesive zone damage-healing model for self-healing materials, Eng. Fract. Mech. 163 (2016) 1–22.
[36] S.A. Ponnusami, J. Krishnasamy, S. Turteltaub, S. van der Zwaag, A cohesive-zone crack healing model for self-healing materials, Int. J. Solids Struct. 134 (2018) 249–263.
[37] A.D. Jefferson, B.L. Freeman, A crack-opening-dependent numerical model for self-healing cementitious materials, Int. J. Solids Struct. 244 (2022) 111601.
[38] Y. Sun, L. Simonini, C. Xing, L. Mishnaevsky Jr, Self-healing interfaces in fiber reinforced polymers: computational modeling, Compos. Sci. Technol. (2025) 111269.
[39] J.S. Turicek, V. Kamala, K.B. Nakshatrala, G. Haikal, J.F. Patrick, Tailoring interlaminar shear and mode-I fracture behavior in fiber-composites via soft self-healing thermoplastic inclusions, Compos. Part A: Appl. Sci. Manuf. 194 (2025) 108803.
[40] T. Zhelyazov, Finite-Element Analysis of the Quasi-Static Response of Concrete Specimens Containing Polymeric Self-Healing Microcapsules, Polymers 18 (11) (2026) 1289.
[41] J. Hanna, A. Elamin, Computational fracture modeling for effects of healed crack length and interfacial cohesive properties in self-healing concrete using XFEM and cohesive surface technique, Computation 11 (7) (2023) 142.
[42] S. Sayadi, I. Mihai, A. Jefferson, Rate dependent self-healing model for cementitious materials, Int. J. Solids Struct. 309 (2025) 113196.
[43] A. Vedrtnam, K. Kalauni, M.T. Palou, Finite element simulation of bacterial self-healing in concrete using microstructural transport and precipitation modeling, Sci. Rep. 15 (1) (2025) 15809.
[44] A. Sadighi, S. Kerrane, H.W. Lee, L. Meng, M.H. Khaneghahi, S.A. Rahmaninezhad, A.R. Najafi, Phase-field modeling of fracture and healing in BioFiber-reinforced concrete, Int. J. Mech. Sci. 301 (2025) 110447.
[45] A. Vedrtnam, M.T. Palou, H. Varela, D. Gunwant, K. Kalauni, G. Barluenga, Experimental and numerical study on post-fire self-healing concrete for enhanced durability, Sci. Rep. 15 (1) (2025) 9731.
[46] T. Maeda, T. Osada, S. Ozaki, Novel numerical approach for reliability-assurance of ceramics by combining self-crack-healing with proof testing, J. Eur. Ceram. Soc. 44 (4) (2024) 2261–2270.
[47] Y. Lim, M.S. Song, S. Ha, Spatium: an open-source Abaqus/CAE plug-in for computational homogenization of particle-reinforced composites, SoftwareX 31 (2025) 102219.
[48] S. Schmauder, L. Mishnaevsky, Micromechanics and Nanosimulation of Metals and Composites: Advanced Methods and Theoretical Concepts, Springer Science & Business Media, 2008.

[49] Q.D. Yang, M.D. Thouless, Mixed-mode fracture analyses of plastically-deforming adhesive joints, Int. J. Fract. 110 (2) (2001) 175–187.
[50] P.W. Harper, S.R. Hallett, A fatigue degradation law for cohesive interface elements–development and application to composite materials, Int. J. Fatigue 32 (11) (2010) 1774–1787.
[51] J.P.H. Belnoue, S.R. Hallett, Cohesive/adhesive failure interaction in ductile adhesive joints Part I: a smeared-crack model for cohesive failure, Int. J. Adhes. Adhes. 68 (2016) 359–368.